Nonlinear photon-atom coupling with 4Pi microscopy

Yue-Sum Chin,[1] Matthias Steiner,[1,2] and Christian Kurtsiefer[1,2]

[1] *Centre for Quantum Technologies, 3 Science Drive 2, Singapore 117543*
[2] *Department of Physics, National University of Singapore, 2 Science Drive 3, Singapore 117542*

(Dated: June 9, 2017)

We present a robust technique to realize photon-atom interaction strong enough to enter the nonlinear regime. The incident photons are tightly focused onto a single atom by adapting a super-resolution imaging technique, 4Pi microscopy. In this configuration the incident beam is split, and the atom is coherently illuminated by two counter-propagating parts of the field. In a proof-of-principle experiment, we demonstrate that in the 4Pi arrangement the interaction is close to doubled compared to one-sided illumination. We observe 36.6(3)% extinction of the incident field, and a modified photon statistics of the transmitted field – indicating nonlinear interaction at the single-photon level. Our results pave the way to few-photon nonlinear optics with individual atoms in free space.

I. INTRODUCTION

Implementing nonlinear interactions between single photons and single atoms is at the forefront of optical physics. Motivated by the prospects of deterministic all-optical quantum logic, many efforts are currently underway to find suitable experimental techniques [1–3]. So far the conceptually simple approach of focusing the photons onto the atom with a lens has yielded only moderate interaction strengths [4–10]. Consequently much attention has been directed to explore other methods to enhance the interaction strength, in particular by coupling the atom to a waveguide [11] or an optical resonator [12]. However, in this work we show that nonlinear interactions at the single-photon level can be realized in free space, i.e., in the absence of waveguides and resonators, by using a different focusing geometry.

For strong free space interaction the photons need to be tightly focused to a small volume [13, 14]. From high-resolution imaging it is well-known that a small focal volume requires optical elements which cover a large fraction of the solid angle [15]. While standard confocal optical microscopy accomplished already very small probe volumes, the excitation light is focused through a lens that can cover only up to half of the solid angle, limiting the axial resolution due to a focal volume elongated along the optical axis. This limitation has been overcome by using two opposing lenses with coinciding focal points, known as 4Pi arrangement [16]: The path of the incident beam is split, and the object is coherently illuminated by two counter-propagating parts of the field simultaneously [see Fig. 1(a)]. In this way the input mode covers almost the entire solid angle, limited only by the numerical aperture of the focusing lenses. The symmetry between imaging and excitation of quantum emitter suggests that a 4Pi arrangement can also be used to efficiently couple light to an atom. This intuitive argument is confirmed by numerical simulations of the electric field distribution near the focal point, from which we obtain the spatial mode overlap of the atomic dipole mode with the input mode, referred to as the light-atom coupling efficiency $\Lambda = |E_{\mathrm{focus}}|^2/|E_{\mathrm{max}}|^2$, where $E_{\mathrm{focus(max)}}$ is the (maximally possible) amplitude of the incident electric field component parallel to the atomic dipole [see Fig. 1(b)-(f)] [17, 18].

II. EXPERIMENTAL SETUP

In our experiment, we hold a single ^{87}Rb atom between two lenses with a far off-resonant optical dipole trap (FORT) operating at a wavelength 851 nm [19]. We compare 4Pi and one-sided illumination by performing a transmission experiment with a weak coherent field driving the closed transition $5S_{1/2}$, F=2, m_F=-2 to $5P_{3/2}$, F=3, m_F=-3 near 780 nm [10]. The probe beam originates from a collimated output of a single mode fiber. After splitting into path 1 and path 2, the beam is focused onto the atom through lenses L_1 and L_2 [see Fig. 1(a)]. The opposing lens re-collimates the probe beam, which is then via an asymmetric beam splitter coupled into a single mode fiber connected to avalanche photodetector D_1 or D_2, respectively (see Appendix A for details). The electric fields at the detectors are superpositions of the probe field and the field scattered by the atom. To derive the total electric field, we adapt the theoretical description of Ref. [17, 20] to account for the contributions of the two counter-propagating probe fields. The optical power P_1 at detector D_1 depends then on the power in the individual beam paths $P_{1(2),\mathrm{in}}$ and the light-atom coupling efficiency $\Lambda_{1(2)}$ of path 1(2),

$$P_1 = \left(\sqrt{P_{1,\mathrm{in}}} - 2\Lambda_1\sqrt{P_{1,\mathrm{in}}} - 2\sqrt{\Lambda_1\Lambda_2}\sqrt{P_{2,\mathrm{in}}}\right)^2, \quad (1)$$

where we assume that the two fields interfere constructively at the focal point. Similarly, the power at detector D_2 is obtained by exchanging subscripts $1 \leftrightarrow 2$. From Eq. (1) we obtain the expected values for the individual transmission $T_{1(2)} = P_{1(2)}/P_{1(2),\mathrm{in}}$, and the total transmission $T_{\mathrm{total}} = (P_1 + P_2)/(P_{1,\mathrm{in}} + P_{2,\mathrm{in}})$. For example, for a one-sided illumination through lens L_1, i.e. $P_{2,\mathrm{in}} = 0$, the transmission measured at detector D_1

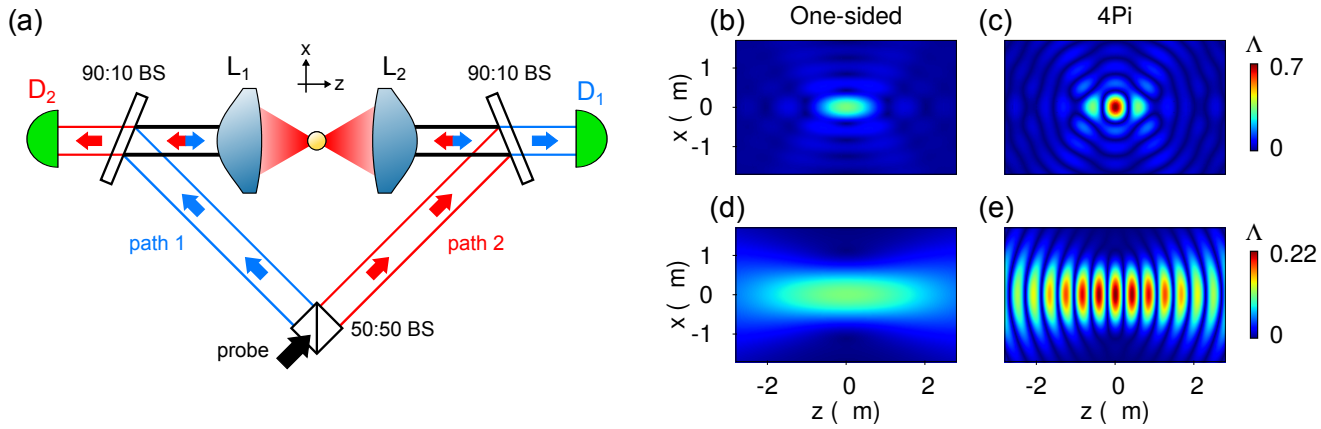

FIG. 1. **Concept of 4Pi illumination.** (a) Schematics of the optical setup. The probe beam (black arrow) is split into path 1 (blue arrows) and path 2 (red arrows). The two beams then illuminate the atom from counter-propagating directions. Asymmetric beamsplitters are used to sample the probe light after passing the atom. The probe light in path 1(2) is coupled into a single mode fiber connected to detector $D_{1(2)}$. By blocking one path, we recover the commonly employed one-sided illumination. BS: beam splitter, $L_{1(2)}$: high numerical aperture lens, $D_{1(2)}$: avalanche photodetector. (b)-(e) Numerical results of the coupling efficiency Λ near the focal point considering a Gaussian field resonantly driving a circularly polarized dipole transition near 780 nm [17]. The field is assumed to constructively interfere at the focal point for the 4Pi configuration. (b)-(c) Focusing parameters corresponding to an objective with numerical aperture NA= 0.95. (d)-(e) Focusing parameters used in this experiment (input beam waist $w_0 = 2.7$ mm at lens, focal length $f = 5.95$ mm).

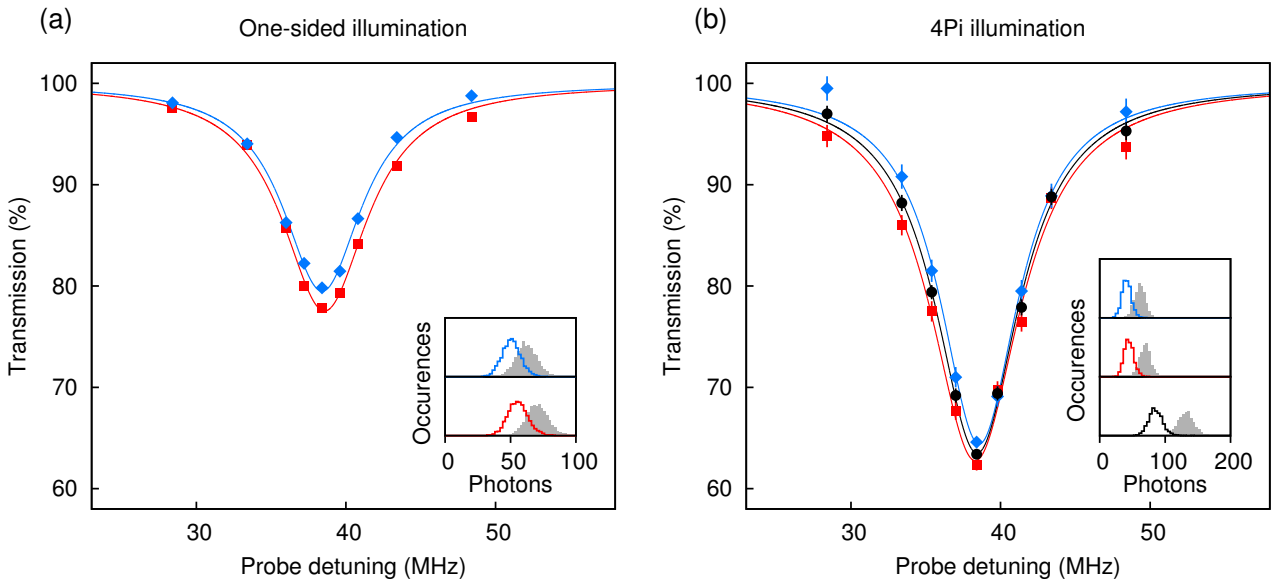

FIG. 2. **Extinction of a weak coherent probe beam.** (a) One-sided illumination via path 1 (blue diamonds) or path 2 (red squares). Solid lines are Lorentzian fits. The inset shows the normalized histogram of detected photons during the probe cycle (solid line) and reference cycle (gray) for the resonant data point. (b) Same as (a) but with 4Pi illumination. The total transmission (black circles) is obtained from the sum of detectors D_1 and D_2. Error bars represent one standard deviation of propagated Poissonian counting uncertainties. The FORT shifts the resonance frequency by approximately 38.5 MHz compared to the natural transition frequency.

takes the well known expression $T_1 = (1 - 2\Lambda_1)^2$ [17, 20]. In the 4Pi configuration, we determine the total coupling Λ_{total} from the total transmission $T_{\text{total}} = (1 - 2\Lambda_{\text{total}})^2$. From Eq. (1) we find that the power splitting $P_{2,\text{in}} = P_{1,\text{in}}\Lambda_1/\Lambda_2$ optimizes the total coupling to $\Lambda_{\text{total}} = \Lambda_1 + \Lambda_2$.

III. EXTINCTION EXPERIMENT

Figure 2(a) shows the transmission spectrum of a weak coherent field for one-sided illumination, either via path 1 (blue) or path 2 (red). Comparing the resonant transmission $T_1 = 77.9(2)\%$ and $T_2 = 79.8(3)\%$ to Eq. (1),

we find similar coupling efficiencies, $\Lambda_1 = 0.059(1)$ and $\Lambda_2 = 0.053(1)$, as expected for our symmetric arrangement with two nominally identical lenses. Therefore, the maximum coupling expected in the 4Pi configuration is $\Lambda_{\text{total}} = \Lambda_1 + \Lambda_2 = 0.112(4)$, assuming perfect phase matching of the fields and ideal positioning of the atom.

In the 4Pi configuration the atom needs to be precisely placed at an anti-node of the incident field [see Fig. 1(e)]. To this end, we tightly confine the atom along the optical axis with an additional blue-detuned standing wave dipole trap (761 nm). As the atom is loaded probabilistically into the optical lattice, we use a simple postselection technique to check whether the atom is trapped close to an anti-node of the incident field (see Appendix B). Figure 2(b) shows the observed transmission when the atom is illuminated in the 4Pi arrangement. The increased light-atom coupling is evident from the strong reduction of transmission. The individual transmissions $T_1 = 62.3(5)\%$, $T_2 = 64.6(5)\%$, and the total transmission $T_{\text{total}} = 63.4(3)\%$ are significantly lower compared to the one-sided illumination. The corresponding total coupling of $\Lambda_{\text{total}} = 0.102(1)$ is close to the theoretical prediction of 0.112(4).

We next show that for a symmetric arrangement $\Lambda_1 \approx \Lambda_2$, the highest interaction is achieved with an equal power splitting $P_{2,\text{in}} \approx P_{1,\text{in}}$. Figure 3 displays the resonant transmissions for different relative beam power in the two paths. For imbalanced beam power, the total transmission is increased, albeit with a fairly weak dependence. In contrast, we find a strong dependence of the individual transmissions on the relative beam power: For $P_{1,\text{in}} \approx 12P_{2,\text{in}}$, the total transmission is still low, $T_{\text{total}} = 71.2(8)\%$, but the two values for the individual transmissions are no longer equal: $T_{1,4\text{Pi}} = 74.0(8)\%$, $T_{2,4\text{Pi}} = 41(2)\%$, in qualitative agreement with Eq. (1) (solid lines in Fig. 3).

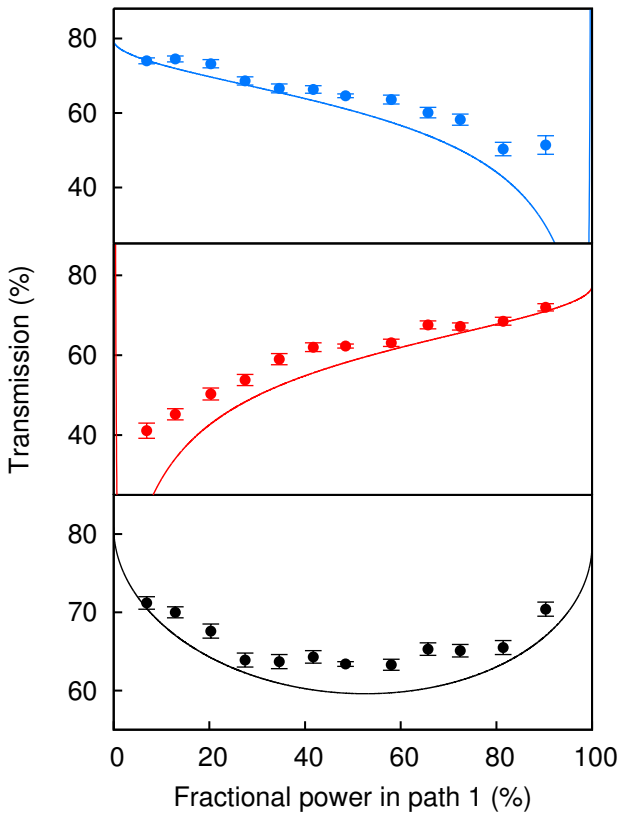

FIG. 3. **Resonant transmission for different power splittings between path 1 and path 2.** Transmission at detector D_1 (top), D_2 (center) and the total transmission $D_1 + D_2$ (bottom). The total number of incident photons is kept constant. Solid lines are $T_{1(2)}$ and T_{total} derived from Eq. (1). Error bars represent one standard deviation of propagated Poissonian counting uncertainties.

IV. SIGNATURE OF NONLINEAR INTERACTION IN PHOTON STATISTICS

The nonlinear character of the photon-atom interaction can induce effective attractive or repulsive interactions between two photons [21]. These interactions can be observed as modification of the photon statistics of the transmitted field if the initial field contains multi-photon contributions [22–26]. For a weak coherent driving field, the second-order correlation function $g^{(2)}(\tau)$ takes the specific form [27, 28]

$$g^{(2)}(\tau) = e^{-\Gamma_0\tau}\left(\left(\frac{2\Lambda}{1-2\Lambda}\right)^2 - e^{\frac{\Gamma_0\tau}{2}}\right)^2, \qquad (2)$$

where $\Gamma_0 = 2\pi \times 6.07\,\text{MHz}$ is the excited state linewidth. By time-tagging the detection events at detector D_1 and D_2 during the probe phase, we obtain $g^{(2)}(\tau) = \langle p_1(t)p_2(t+\tau)\rangle / (\langle p_1(t)\rangle\langle p_2(t+\tau)\rangle)$, where $p_{1(2)}(t)$ is the detection probability at detector $D_{1(2)}$ at time t, and $\langle\rangle$ denotes the long time average. To acquire sufficient statistics, we use 50% more photons in the probe pulse as compared to Fig. 2, and also atoms which are not optimally coupled to the probe field (see Appendix B). From the resulting average transmission $T_{\text{total}} = 70.3(3)\%$, we deduce an average coupling $\Lambda_{\text{total}} = 0.0808(5)$ for this experiment. As shown in Fig. 4, we find a clear signature of nonlinear photon-atom interaction in the intensity correlations of the transmitted light. The observed photon anti-bunching $g^{(2)}(0) = 0.934(7)$ is in good agreement with Eq. (2). Here, for fair comparison with Eq. (2), we account for a small photon bunching effect ($\approx 1.7\%$, see Appendix C) due to the diffusive atomic motion [29, 30]. For stronger light-atom coupling the changes of the photon statistics are expected to be more significant [see Fig. 4(b)]. Notably, for $\Lambda = 0.25$ the transmitted and the reflected light show anti-bunching ($g^{(2)}(0) = 0$), that means the atom acts as a photon turnstile and converts a coherent field completely into a single photon field. The transmission for this light-atom coupling is $T_{\text{total}} = 25\%$

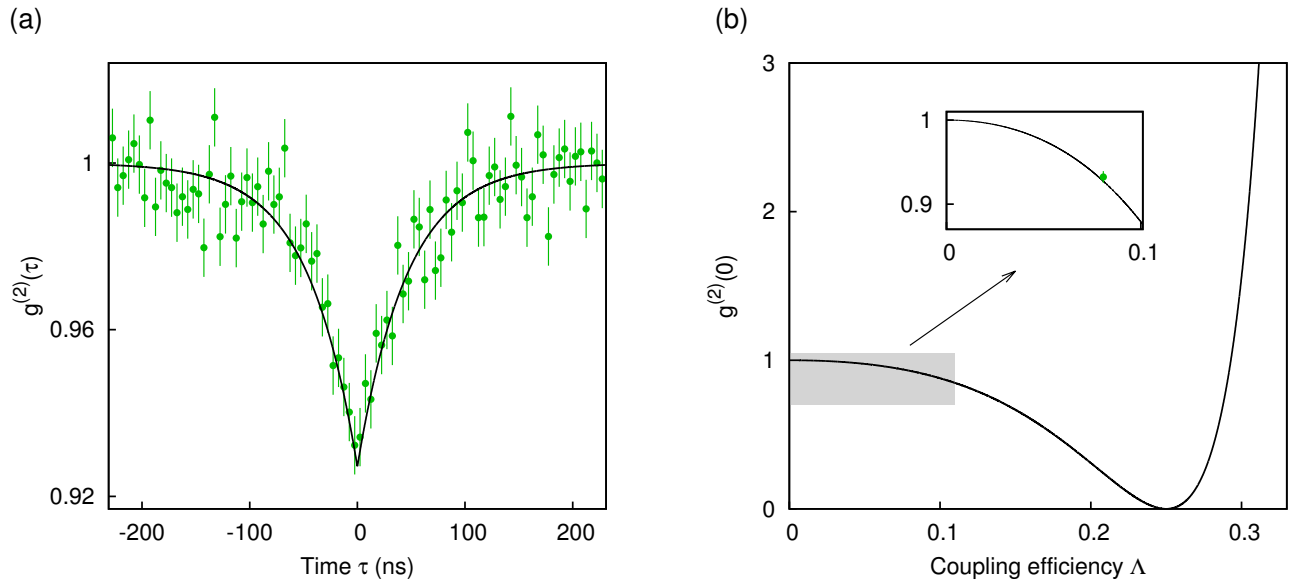

FIG. 4. **Modified photon statistics due to nonlinear interaction.** (a) Intensity correlation of transmitted light with a time bin width of 5 ns. Solid line is the theoretical prediction without free parameter [see Eq. (2)]. (b) Dependence on the coupling efficiency Λ. The inset is a zoom into the region of our data point for clarity, and the solid line is $g^{(2)}(0)$ from Eq. (2).

[see Eq. (1)]. Photon bunching ($g^{(2)}(0) > 1$) for large values of Λ signals an enhanced probability for multiple photons to be transmitted, essentially because the atom cannot scatter multiple photons simultaneously.

V. DISCUSSION AND OUTLOOK

Our work establishes the 4Pi arrangement as an effective technique to couple a propagating field to an atom. This opens exciting prospects to implement effective interactions between photons with tightly focused free space modes and single atoms. Strongly interacting photons could find application in imaging, metrology, quantum computing and cryptography, and constitute a novel platform to study many-body physics [31, 32].

The presented approach forms an experimental alternative to waveguide/cavity quantum electrodynamics [12, 22] and Rydberg quantum optics [26, 33, 34]. For a comparison to waveguide/cavity systems we consider the Purcell factor P as a measure for the light-atom interaction strength. For an atom with spontaneous emission rates Γ_{system} into the cavity/waveguide and Γ_{env} into uncontrolled modes belonging to the environment, the Purcell factor is defined as $P = \Gamma_{\text{system}}/\Gamma_{\text{env}}$ where a Purcell factor above unity signals strong light-atom coupling. In waveguide/cavity systems strong coupling is achieved by increasing Γ_{system} while $\Gamma_{\text{env}} \approx \Gamma_0$ remains close to the natural spontaneous emission rate. In contrast in a free space experiment these rate are directly coupled, $\Gamma_{\text{system}} = \Lambda\Gamma_0$ and $\Gamma_{\text{env}} = (1-\Lambda)\,\Gamma_0$. Hence Purcell factors above unity are also possible in free space. For example, for a 4Pi configuration with lenses of numerical aperture 0.95 [see Fig.1(c)] the Purcell factor is $P \approx 2.3$. Other free space focusing geometries could implement even larger Purcell factors [13]. However, the advantage of the 4Pi arrangement is that it can be realized with off-the-shelf high numerical aperture objectives and avoids the technical overhead associated with cavities and waveguides.

While the achieved nonlinearity of the photon-atom interaction, observed as modification of the photon statistics, does not create strongly correlated photons yet, the 4Pi arrangement eases the technical requirements to the focusing lens considerably, making the implementation of strong photon-photon interaction feasible. In the near future, we expect that by using higher numerical aperture lenses, the 4Pi arrangement will allow the efficient conversion of a coherent beam into single photons.

ACKNOWLEDGMENTS

We acknowledge the support of this work by the Ministry of Education in Singapore (AcRF Tier 1) and the National Research Foundation, Prime Minister's office. M. Steiner acknowledges support by the Lee Kuan Yew Postdoctoral Fellowship.

Appendix A: OPTICAL SETUP

Figure 5 shows the optical setup. The Gaussian probe beam is delivered from a single-mode fiber, collimated and split into two paths. The power ratio in the two paths is controlled by a half-wave plate and a polariz-

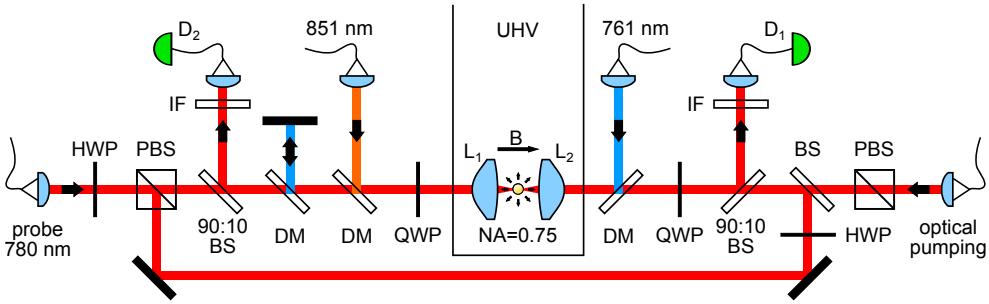

FIG. 5. **Optical setup.** D_1, D_2: avalanche photodetectors (APDs), IF: interference filter, HWP, QWP: half- and quarter-wave plates, (P)BS: (polarizing) beam splitter, DM: dichroic mirror, L_1, L_2: high numerical aperture lenses, B: magnetic field, UHV: ultra-high vacuum chamber.

ing beam splitter. Half- and quarter-wave plates ensure the same polarization (σ^-) in both paths at the position of the atom. After passing through the lens pair, the probe light is coupled into single mode fibers connected to avalanche photodetectors. We optimize the fiber couplings to collect the probe light and measure 40% coupling loss that is due to imperfect mode matching.

We trap single ^{87}Rb atoms with a red-detuned far-off-resonant dipole trap (FORT) at 851 nm. The circularly polarized (σ^+) beam is focused to a waist $w_0 \approx 1.4\,\mu$m, which results in a trap depth of $U_0 = k_B \times 1.88\,$mK. The position of the trap is adjusted to maximize the collected atomic fluorescence at the detectors D_1 and D_2. In addition, we use a blue-detuned FORT at 761 nm in standing wave configuration overlapping with the red-detuned FORT to increase the axial confinement. The blue-detuned FORT is linearly polarized and has a trap depth of approximately 0.1 mK along the optical axis.

Appendix B: EXPERIMENTAL SEQUENCE AND POSTSELECTION OF ATOM POSITION

Measurement strategy. To fully utilize the 4Pi arrangement the atom needs to placed at an anti-node of the probe field. Unfortunately, the interference pattern of the probe field changes over time owing to slow drifts in the optical path lengths. The probe-atom coupling is further affected by similar drifts of the optical lattice, and the probabilistic loading into particular lattice sites. Here we exploit that once an atom is loaded, the timescale for a transmission experiment is much shorter (milliseconds) than the timescale of the drifts (minutes). Therefore, each experimental cycle consists of two independent transmission experiments: one to check whether the atom is trapped at the right position and one to determine the light-atom interaction. In the actual sequence we first perform the light-atom interaction experiment before checking the atom position. In this way we minimize the effect of recoil heating from the probe field.

Experimental sequence. The experiment begins upon the loading of a single atom. We then perform polarization gradient cooling for 5 ms (Fig. 6), which cools the atom to a temperature of about 16 μK. A bias magnetic field of 0.74 mT is applied along the optical axis, and the atom is prepared in the $5S_{1/2}$, F=2, m_F=-2 state by optical pumping. Next, two probe fields are applied each for 1 ms, separated by a 4 μs pause. We tune the frequency of the first probe, for example, to obtain the transmission spectra shown in Fig. 2. The second probe cycle is used to check whether the atom has been trapped at an anti-node of the probe field. For this, the frequency of the probe field is set to be resonant with the atomic transition. Subsequently, we perform a reference measurement to obtain the instantaneous probe power. We first optically pump the atom to the $5S_{1/2}$, F=1 hyperfine state, shifting the atom out of resonance with the probe field by 6.8 GHz, after which we reapply the two probe fields. The detection events at avalanche photodetectors D_1 and D_2 are recorded during all probe cycles.

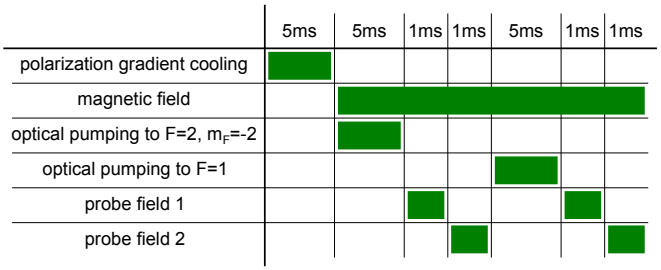

FIG. 6. **Experimental sequence.**

Postselection of atom position. We illustrate the postselection procedure for the case in which the probe field during the first probe cycle is resonant with the atomic transition. Figure 7a/b shows the histogram of detected photons in the first/second probe cycle. The position of the atom is postselected based on the detected transmission during the second probe cycle. For an atom loaded into a desired site of the potential well, the transmission is low. Hence, we discard detection events in the first probe cycle if the number of photons detected in the second cycle is above a threshold value. Figure 7c shows the histogram of detected photons in the first probe cycle

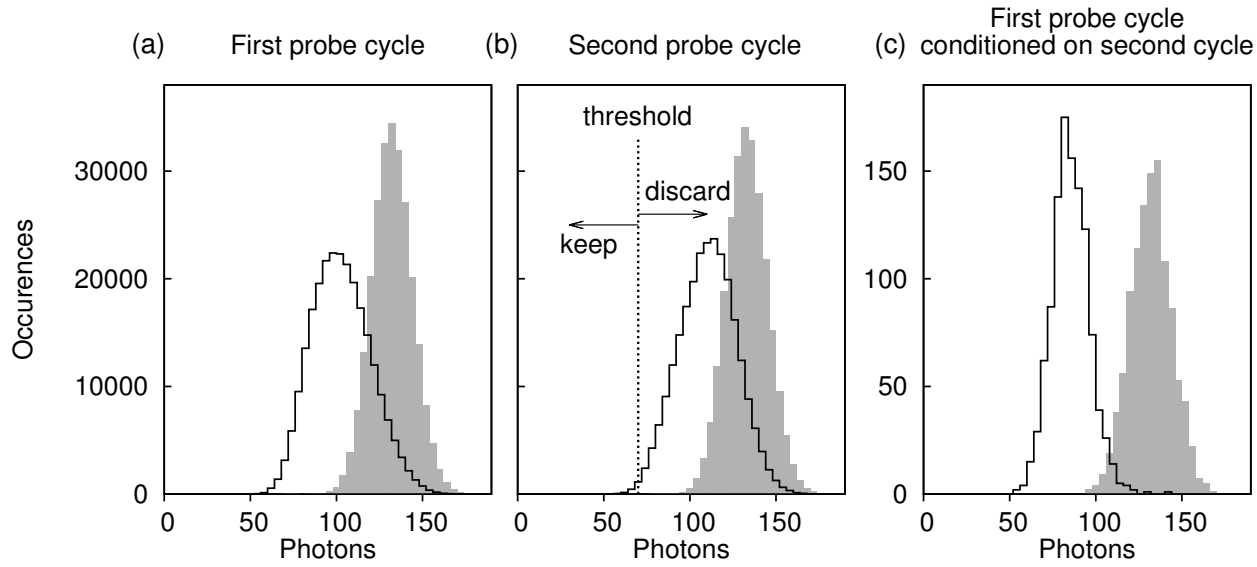

FIG. 7. **Postselection of atom position.** Photon counting histogram recorded during probe (solid line) and reference (gray) cycle. The total number of detected photons is computed as the sum of detectors D_1 and D_2. (a) First probe cycle for the case when the probe field is resonant to the atomic transition. (b) Second probe cycle. The dotted line marks the set threshold for a postselection of approximately 0.5% of the total events. (c) Resultant events of the first probe cycle conditioned on the second cycle using the marked threshold in **b**.

after postselection. For the transmission measurements shown in Fig. 2 and Fig. 3, we use a photocount threshold that selects approximately 0.5% of the total events, trading off between data acquisition rate and selectiveness of the atomic position. For the case of one-sided illumination, this postselection procedure does not change the observed transmission. In the second order correlation measurement, we use a higher threshold value to speed up the data acquisition, selecting 10% of the total events. The correlations shown in Fig. 4 are the result of approximately 200 hours of measurement time.

Appendix C: NORMALIZATION OF SECOND ORDER CORRELATION FUNCTION

We compute the second order correlation function from the time-tagged photodetection events at detector D_1 and D_2. We sort the photodetection events into a time delay histogram and obtain the normalized correlation function by dividing the number of occurrences by $r_1 r_2 \Delta t T$, where $r_{1(2)}$ is the mean count rate at detector $D_{1(2)}$, Δt is the time bin width and T is the total measurement time. To make the normalization robust against intensity drifts of the probe power, we perform the normalization for every 1 ms-long measurement cycle, obtaining the normalized correlation function $g_i^{(2)}(\tau)$ (index i describes the measurement cycle) and then $g^{(2)}(\tau)$ from the weighted mean

$$g^{(2)}(\tau) = \frac{\sum_{i=1}^{N} g_i^{(2)}(\tau)(r_{1,i} + r_{2,i})}{\sum_{i=1}^{N}(r_{1,i} + r_{2,i})}. \qquad \text{(C1)}$$

Figure 8(a)-(b) shows $g^{(2)}(\tau)$ around $\tau = 0$ and for longer time delays. For large τ, the correlation disappears, and $g^{(2)}(\tau)$ approaches unity. However, for $100\,\text{ns} < \tau < 1\,\mu\text{s}$, $g^{(2)}(\tau)$ shows super-Poissonian intensity correlations $g^{(2)}(\tau) > 1$. Similar correlations have been observed in the fluorescence of single atoms in dipole traps induced by the atomic motion through the trap (Ref. [29, 30]).

Although the amplitude of the correlations is small, we nevertheless perform a deconvolution for a better comparison to Eq. (2). For diffusive motion the correlations are expected to decay exponentially, thus we fit $f(\tau) = 1 + a_0 \exp(-\tau/\tau_d)$ to $g^{(2)}(\tau)$, resulting in $a_0 = 0.019(2)$, $\tau_d = 0.71(8)\,\mu\text{s}$, with a reduced $\chi^2 = 1.07$ (see Figure 8(b), black solid line). We note that the timescale τ_d of these correlations is much larger than the excited state lifetime $1/\Gamma_0 = 26.2\,\text{ns}$. Figure 4 shows the second order correlation function corrected for the diffusive motion, i.e. after division by $f(\tau)$. No additional correlations are present in the transmitted light during the reference cycle, i.e., when the atom is not resonant with probe field [see Fig. 8(c)].

[1] T. G. Tiecke, J. D. Thompson, N. P. de Leon, L. R. Liu, V. Vuletic, and M. D. Lukin, Nature **508**, 241 (2014).

[2] I. Shomroni, S. Rosenblum, Y. Lovsky, O. Bechler,

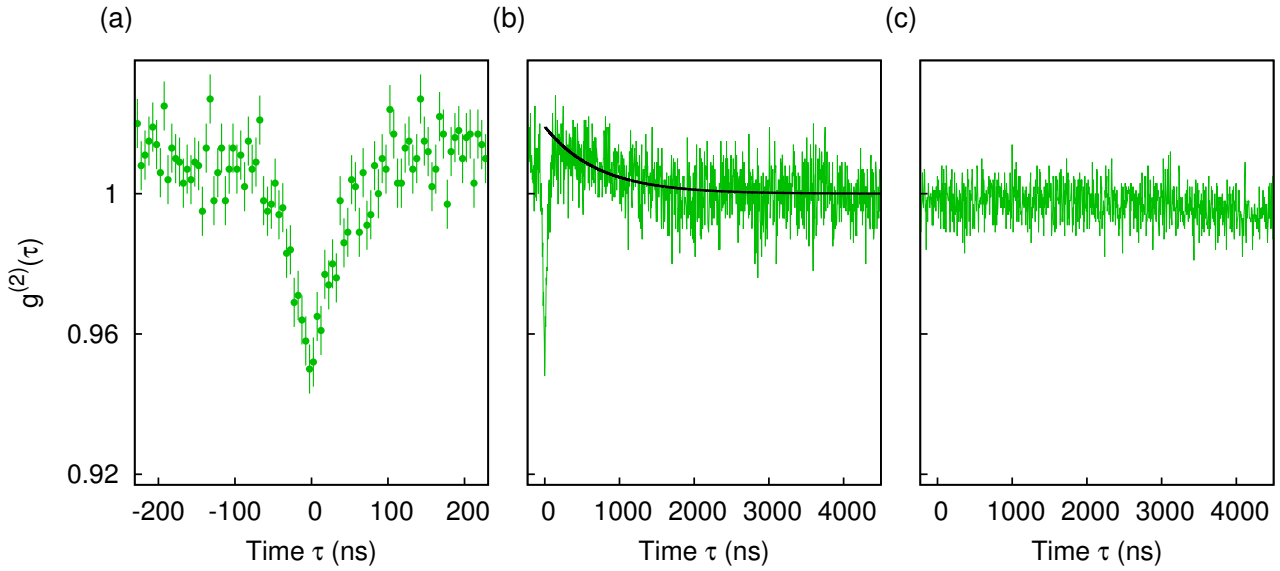

FIG. 8. **Photon bunching due to atomic motion.** (a) Normalized second order correlation function without deconvolution of the diffusive atomic motion. (b) Same as (b) but with extended range. Solid line is a fit to $f(\tau) = 1 + a_0 \exp(-\tau/\tau_d)$ with $a_0 = 0.019(2)$, $\tau_d = 0.71(8)\,\mu$s and a reduced $\chi^2 = 1.07$. (c) Same as (b) but computed from events during the reference cycle, i.e., when the atom is not resonant with probe field.

G. Guendelman, and B. Dayan, Science **345**, 903 (2014).
[3] B. Hacker, S. Welte, G. Rempe, and S. Ritter, Nature **536**, 193 (2016).
[4] D. J. Wineland, W. M. Itano, and J. C. Bergquist, Opt. Lett. **12**, 389 (1987).
[5] A. N. Vamivakas, M. Atatüre, J. Dreiser, S. T. Yilmaz, A. Badolato, A. K. Swan, B. B. Goldberg, A. Imamoğlu, and M. S. Ünlü, Nano Letters **7**, 2892 (2007).
[6] M. K. Tey, Z. Chen, S. A. Aljunid, B. Chng, F. Huber, G. Maslennikov, and C. Kurtsiefer, Nat Phys **4**, 924 (2008).
[7] G. Wrigge, I. Gerhardt, J. Hwang, G. Zumofen, and V. Sandoghdar, Nat Phys **4**, 60 (2008).
[8] N. Piro, F. Rohde, C. Schuck, M. Almendros, J. Huwer, J. Ghosh, A. Haase, M. Hennrich, F. Dubin, and J. Eschner, Nat Phys **7**, 17 (2011).
[9] A. Maser, B. Gmeiner, T. Utikal, S. Götzinger, and V. Sandoghdar, Nat Photon **10**, 450 (2016).
[10] Y.-S. Chin, M. Steiner, and C. Kurtsiefer, Phys. Rev. A **95**, 043809 (2017).
[11] D. Roy, C. M. Wilson, and O. Firstenberg, Rev. Mod. Phys. **89**, 021001 (2017).
[12] A. Reiserer and G. Rempe, Rev. Mod. Phys. **87**, 1379 (2015).
[13] M. Sondermann, R. Maiwald, H. Konermann, N. Lindlein, U. Peschel, and G. Leuchs, Applied Physics B **89**, 489 (2007).
[14] G. Leuchs and M. Sondermann, Journal of Modern Optics **60**, 36 (2012).
[15] E. Abbe, Archiv für mikroskopische Anatomie **9**, 413 (1873).
[16] S. Hell and E. H. K. Stelzer, J. Opt. Soc. Am. A **9**, 2159 (1992).
[17] M. K. Tey, G. Maslennikov, T. C. H. Liew, S. A. Aljunid, F. Huber, B. Chng, Z. Chen, V. Scarani, and C. Kurtsiefer, New Journal of Physics **11**, 043011 (2009).
[18] A. Golla, B. Chalopin, M. Bader, I. Harder, K. Mantel, R. Maiwald, N. Lindlein, M. Sondermann, and G. Leuchs, The European Physical Journal D **66**, 190 (2012).
[19] N. Schlosser, G. Reymond, I. Protsenko, and P. Grangier, Nature **411**, 1024 (2001).
[20] L. Slodička, G. Hétet, S. Gerber, M. Hennrich, and R. Blatt, Phys. Rev. Lett. **105**, 153604 (2010).
[21] J.-T. Shen and S. Fan, Phys. Rev. Lett. **98**, 153003 (2007).
[22] K. M. Birnbaum, A. Boca, R. Miller, A. D. Boozer, T. E. Northup, and H. J. Kimble, Nature **436**, 87 (2005).
[23] B. Dayan, A. S. Parkins, T. Aoki, E. P. Ostby, K. J. Vahala, and H. J. Kimble, Science **319**, 1062 (2008).
[24] A. Reinhard, T. Volz, M. Winger, A. Badolato, K. J. Hennessy, E. L. Hu, and A. Imamoğlu, Nat Photon **6**, 93 (2012).
[25] I.-C. Hoi, T. Palomaki, J. Lindkvist, G. Johansson, P. Delsing, and C. M. Wilson, Phys. Rev. Lett. **108**, 263601 (2012).
[26] T. Peyronel, O. Firstenberg, Q.-Y. Liang, S. Hofferberth, A. V. Gorshkov, T. Pohl, M. D. Lukin, and V. Vuletic, Nature **488**, 57 (2012).
[27] D. E. Chang, A. S. Sorensen, E. A. Demler, and M. D. Lukin, Nat Phys **3**, 807 (2007).
[28] H. Zheng, D. J. Gauthier, and H. U. Baranger, Phys. Rev. A **82**, 063816 (2010).
[29] V. Gomer, B. Ueberholz, S. Knappe, F. Strauch, D. Frese, and D. Meschede, Applied Physics B **67**, 689 (1998).
[30] M. Weber, J. Volz, K. Saucke, C. Kurtsiefer, and H. Weinfurter, Phys. Rev. A **73**, 043406 (2006).
[31] D. E. Chang, V. Gritsev, G. Morigi, V. Vuletic, M. D. Lukin, and E. A. Demler, Nat Phys **4**, 884 (2008).

[32] D. E. Chang, V. Vuletic, and M. D. Lukin, Nat Photon **8**, 685 (2014).
[33] J. D. Pritchard, D. Maxwell, A. Gauguet, K. J. Weatherill, M. P. A. Jones, and C. S. Adams, Phys. Rev. Lett. **105**, 193603 (2010).
[34] O. Firstenberg, C. S. Adams, and S. Hofferberth, Journal of Physics B: Atomic, Molecular and Optical Physics **49**, 152003 (2016).